Supplementary information: Tension tuning of sound and heat transport in graphene

H. Liu[1], M. Lee[2], M. Šiškins[1,2], H. S. J. van der Zant[2], P. G. Steeneken[1,2] and G. J. Verbiest[1]

[1]*Department of Precision and Microsystems Engineering, Delft University of Technology*

[2]*Kavli Institute of Nanoscience, Delft University of Technology*

1 Sample characterization

We use indentation measurements with an atomic force microscope (AFM) to determine the 2D Young's modulus Et of the suspended membranes. This indentation measurement is modelled as a clamped circular membrane with central point loading. The relationship between the applied force F with the AFM cantilever and the resulting deformation δ is given by $F = n_0\pi\delta + Etq^3\delta^3/r^2$, where $q = 1/(1.05 - 0.15\nu - 0.16\nu^2)$ is a geometrical factor with a Poisson's ratio $\nu = 0.16$ (ref.[1]) and n_0 is the pretension in the membrane. We extract Et of our graphene devices through fitting the measured curves of F vs δ. A statistical analysis over 21 different drums in yielded a mean value of Et =$175.39\,\mathrm{N/m}$ (ref.[2]), which is therefore used in equation (3) of the main text to further estimate the induced tension.

2 Readout of the thermodynamic properties

As described in Methods section of the main text, an optomechanical drive allows us to actuate the graphene resonators and measure their thermodynamic properties. For the detection of the motion of the graphene membranes, we use a red laser (λ=633 nm) with a power of $1.2\,\mathrm{mW}$, whereas we use an intensity modulated blue laser (λ=405 nm) with a power P_{ac} of $0.13\,\mathrm{mW}$. We sweep the frequency $\omega/2\pi$ of the intensity modulation from $100\,\mathrm{kHz}$ to $100\,\mathrm{MHz}$. In addition, to correct for intrinsic phase shifts from the interferometric setup, we calibrate the measured signals on the VNA by pointing the blue laser directly onto the photodiode (see more details in ref.[3]). This correction allows us to obtain the real and imaginary part of the membrane motion z_ω as shown in Fig. 1e$-$1g.

The thermal peak observed in the motion of the measured graphene drums are only present in case of an optothermal drive. For other actuation methods, such as an electrostatic and piezoelectric drive, this peak is absent. Also, we reported that the used laser powers in this work have no effect on τ[3,4].

3 Scattering model for acoustic phonons

Acoustic phonons scatter at the kink present in the boundary of the drum with the substrate. The scattering rates depend on the tension in the membrane, speed of the phonons, and the incidence angle. In our experiment, we tune the tension and speed of the phonons and thereby also the measured τ. Fig. S1a illustrates the situation for an incoming flexural phonon at the kink. Domain 1 and domain 2 represent the suspended membrane and the sidewall, respectively. The transmission

probabilities for the different phonon modes ($2j$, $j = l, t, z$) at a given incident angle θ is given by

$$w_{1z\to 2j} = \frac{c_j |u_{2j}|^2 \mathrm{Re}(\cos\theta_{2j})}{c_z |u_{1z}|^2 \cos\theta_{1z}}, j = l, t, z \tag{S1}$$

where $|u_{1z}|$ and $|u_{2j}|$ are wave amplitudes of modes $1z$ and $2j$, respectively. The transmission angle θ_{2j} is determined by Snell's law as $\sin\theta_{2j} = c_{2j}/c_{1z}\sin\theta_{1z}$. We assume a kink angle $\beta = 90°$, in which case $|u_{2j}|$ depends both on tension n and on the speed of flexural phonon c_z (see derivations in ref.[5]).

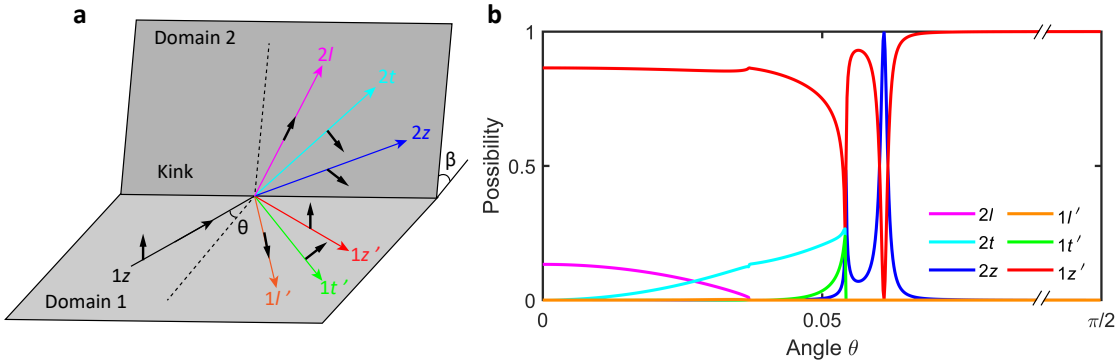

Fig. S1: Phonons scattering at kink in membrane. **a**, Diagram of the scattering model for an incoming flexural phonon (mode $1z$) on the kink. Transmitted and reflected modes are denoted by ($2l$, $2t$, and $2z$) and ($1l'$, $1t'$, and $1z'$), respectively. **b**, Transmission and reflection possibilities as the function of the angle θ of the incoming flexural phonon computed by the full set of equations given in ref.[5]. In this example, we assumed $n = 0.3\,\mathrm{N/m}$ and $c_z = 575\,\mathrm{m/s}$.

Using equation (S1), we plot all transmission and reflection possibilities versus θ (Fig. S1b) for a tension of $n = 0.3\,\mathrm{N/m}$ and $c_z = 575\,\mathrm{m/s}$. The graph shows that transmission of the incoming flexural phonon to the sidewall only occurs when $\theta < 4.29°$. Interestingly, mode $2z$ (blue line) exhibits two peaks at around $3.12°$ and $3.50°$, which are attributed to a resonant transmission of

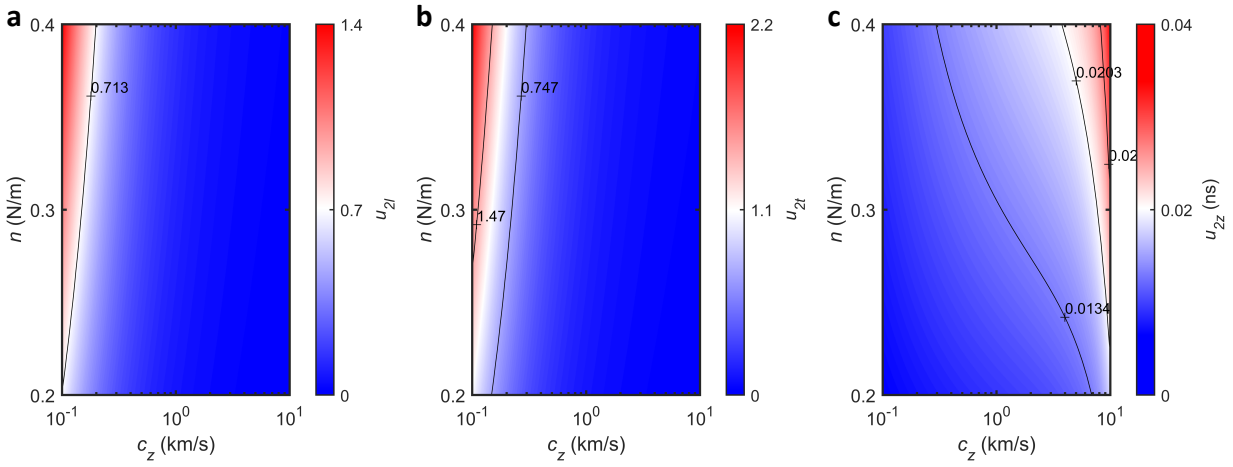

Fig. S2: Transmitted wave amplitudes of three types of acoustic phonons versus the sound speed of flexural phonons c_z and tension n. a−c, Results of $u_{2l}(n, c_z)$, $u_{2t}(n, c_z)$ and $u_{2z}(n, c_z)$, respectively.

waves. On the other hand, since $w_{1z\to1z'} \simeq 1$ when $\theta > 4.29°$, the incident flexural phonons are almost always reflected, which results in a large thermal boundary resistance. We then calculate transmission coefficients $\overline{w}_{1z\to2j}$ $(j = l, t, z)$ through integrating $w_{1z\to2j}$ over the range of θ from $-\pi/2$ to $\pi/2$. Finally, we compute τ as the functions of c_z and n by substituting $\overline{w}_{1z\to2j}$ into equation (3) in the main text.

Using the expression of wave amplitudes of the transmitted modes $2j$ (ref.[5]), we further discuss the dependence of n and c_z on u_{2l}, u_{2l} and u_{2l}, respectively (see Fig. S2). E.g., as tension n increases, the impedance matching between the flexural phonons on suspended membrane and the in-plane phonons on supported membrane is improved, due to a weakening of deflection-induced dilatation and shear, results in the growing amplitudes of u_{2z} mode and further play the role on τ. The increase of c_z will reduce u_{2l} and u_{2t}, and only contribute positively to the flexural mode

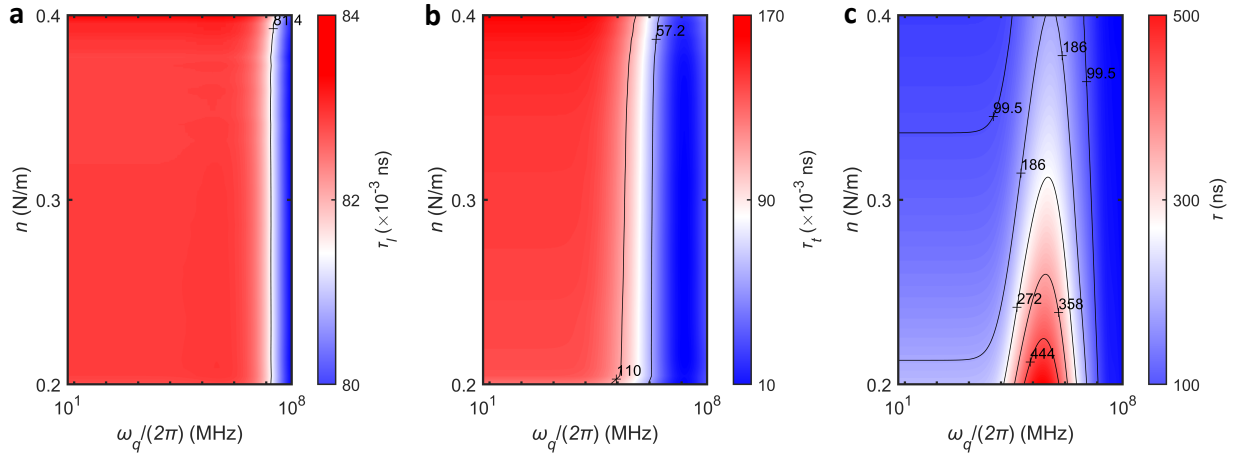

Fig. S3: Thermal time constants of three types of acoustic phonons versus the phonons frequency $\omega_q/2\pi$ and tension n. **a**$-$**c**, Results of $\tau_l(n,\omega_q)$, $\tau_t(n,\omega_q)$ and $\tau(n,\omega_q)$, respectively. In general, the magnitude of $\tau(n,\omega_q)$ is three order larger than that of $\tau_l(n,\omega_q)$ and $\tau_t(n,\omega_q)$, indicating the dominant contribution of flexural phonon on the thermal characterization in graphene. The calculated result in **c** is then weighted by the ω_q-dependent specific heat and obtain the total $\tau(n)$ in theory.

u_{2z}. In general, u_{2l} and u_{2t} are two-order-larger than u_{2z}, showing the intense reflection of flexural phonons at the kink.

Note that equation (S1) and equation (2) in the main text are not only applicable for calculating τ, but also for calculating the thermal time constants τ_l (LA) and τ_t (TA) of the in-plane phonons. Also realize that the speed of sound c_z is a function of the phonon frequency ω_q (see SI section 4) through the dispersion relation of the material. To illustrate these dependencies, we plot $\tau_l(n,\omega_q)$, $\tau_t(n,\omega_q)$ and $\tau(n,\omega_q)$ as a function of both ω_q and n (see Fig. S3). In this example, the parameters of device D4 are used, with a drum radius of r is $5\,\mu\mathrm{m}$ and a bending rigidity κ of $0.6\,\mathrm{eV}$. As

Figs. S3a and S3b show, both τ_l and τ_t decrease as ω_q increases due to Snell's law, but are nearly independent of n. On the contrary, τ exhibits a strong dependence on n (Fig. S3c). Generally speaking, $\tau(n, \omega_q)$ is roughly three orders of magnitude higher than $\tau_l(n, \omega_q)$ and $\tau_t(n, \omega_q)$, which agrees well with flexural phonon dominated the heat transport in graphene[6,7]. The measured τ in our graphene drum devices is therefore equal to weighed average over the contributions of all flexural phonons with frequency ω_q.

4 Debye model of acoustic phonons

Acoustic phonons in graphene exhibit a dispersion relations[8]. In-plane (LA and TA) phonons have a linear dispersion relation $\omega_q = c_j q$ ($j = l, t$), in which q is the wavenumber (see Fig. S4a, left panel). In line with theoretical and experimental work, we use c_l =21.6 km/s and c_t =16 km/s in our calculations[9,10]. On the other hand, flexural acoustic phonons have a nonlinear dispersion relation[11] expressed as $\omega_q = \sqrt{(\kappa q^4 + nq^2)/(\eta \rho_g)}$, where κ is the bending rigidity of the membrane, and η is the normalized areal mass of the membrane extracted from the effective mass density m_{eff} (obtained from the fits in Fig. 2a). The speed of flexural phonons is thus expressed as $c_z = \frac{\partial \omega_q}{\partial q}$. Furthermore, we can obtain the specific heat spectral density $C^z_{v,\omega}$ of flexural phonons in graphene[9]:

$$C^z_{v,\omega} = k_B \left(\frac{\hbar\omega_q}{kT}\right)^2 \frac{e^{\hbar\omega_q/kT}}{\left(e^{\hbar\omega_q/kT} - 1\right)^2} D\left(\omega_q\right) \tag{S2}$$

where k_B is the Boltzmann constant, $\hbar$ is the Planck constant divided by 2π, and $D(\omega_q)$ is the density of states for the given dispersion relations. Using the above equation (S2) We can also obtain the specific heat spectral density $C^j_{v,\omega}$ ($j = l, t$) of in-plane acoustic phonons (see Fig. S4a,

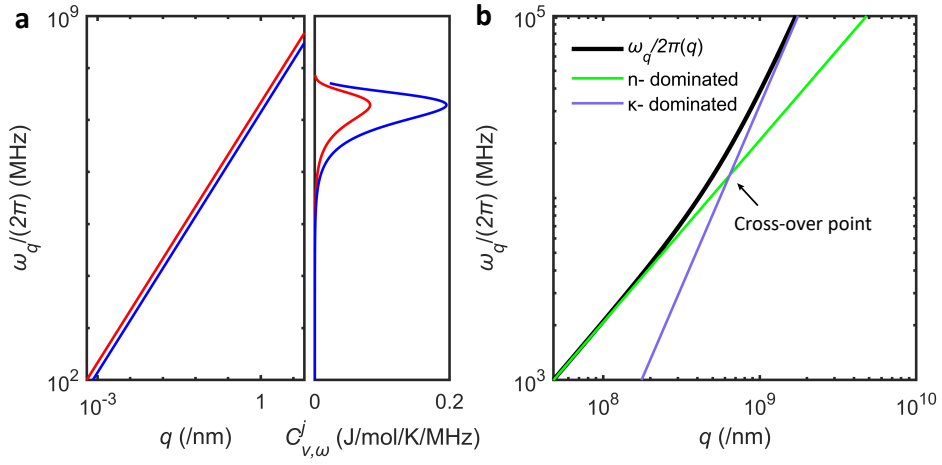

Fig. S4: Calculations for dispersion relation of acoustic phonons. a, Left panel: dispersion relation of in-plane acoustic phonons LA (red line) and TA (blue line); right panel: the corresponding specific heat spectral density $C^j_{v,\omega}$ $(j = l, t)$. **b**, Dispersion relation of flexural phonons for device D1 (black line), using the extracted tension $n = 0.25\,\mathrm{N/m}$, bending rigidity $\kappa = 3.8\,\mathrm{eV}$ and normalized areal mass $\eta = 19.401$ from the main text. The cross-over frequency ω_{qc} corresponds to the transition of dispersion relation from n- dominated regime to κ- dominated regime.

right panel), which are independent to any parameters and remain unchanged in our work.

For the flexural dispersion ω_q, κ dominates the high frequency (THz) regime while n dominates the low frequency (MHz) regime. We define the point where the domination transmits as the cross-over frequency ω_{qc} of dispersion. Through intersecting $\omega_q = q\sqrt{n/(\eta\rho_g)}$ and $\omega_q = q^2\sqrt{\kappa/(\eta\rho_g)}$, we determine ω_{qc} for all devices D1$-$D4, located at 84.8, 52.6, 174.4 and 422.7 GHz, respectively (see Fig. S4b).

Let us now explore the roles κ, η and n play on our Debye scattering model (see Fig. S5). Assume

the initial values of these factors as $\kappa = 0.6\,\mathrm{eV}$, $\eta = 10$ and $n = 0.3\ \mathrm{N/m}$, as well as the radius of membrane $r = 5\,\mu\mathrm{m}$. In terms of $\omega_q(q)$ and c_z, κ and n mainly play the roles on THz and MHz regime, respectively, while η does on both regimes (see Fig. S5a-f). On the other hand, κ and n purely tune the magnitude and the ω_q- distribution of $C^z_{v,\omega}$, separately, while they act on the inverse way for τ (see Fig. S5g-l). It should be noted that the sensitivity of n on τ is extremely higher compared to that of κ and η. Hence, the tunability of τ as observed in our measurements is mainly attributed to the induced n, which directly contributes to the impedance matching of the acoustic phonons at the edge of the membrane.

For each ω_q, the above calculation gives us the thermal time constant and the specific heat spectral density for all types of acoustic phonons and a given tension n. Following the definition of the specific heat, we use a weighing relation as introduced, $1/\tau = \int_0^{\omega_{qd}} C^i_{v,\omega}(\omega_q)/(C^i_v\tau(\omega_q))\mathrm{d}\omega_q$, where $C^i_v = \int_0^{\omega_{qd}} C^i_{v,\omega}(\omega_q)\mathrm{d}\omega_q$ is the total specific heat of a particular phonon type $i = l, t, z$, to separately obtain τ, τ_l and τ_t. Following the flow chart depicted in Fig. 3a of the main manuscript, κ is the only fitting parameter to match the calculated to the measured τ.

We further discuss the role of κ played on the tension-dependent tunable τ (Fig. S6). It shows that as κ goes up from 0.6 to $19\,\mathrm{eV}$, the magnitude of τ is improved obviously. This can be explained that the increase of κ leads to the decrease of c_z (Fig. S5d) as well as the increase of $C^z_{v,\omega}$ (Fig. S5d). The former will cause the decrease of transmitted amplitude in scattering model (see Fig. S2), while the latter will directly improve the weighed factors of τ, both of which will result in the enhancement of τ. In addition, we also observe the slope $|\partial\tau/\partial n|$ increases with κ at the same

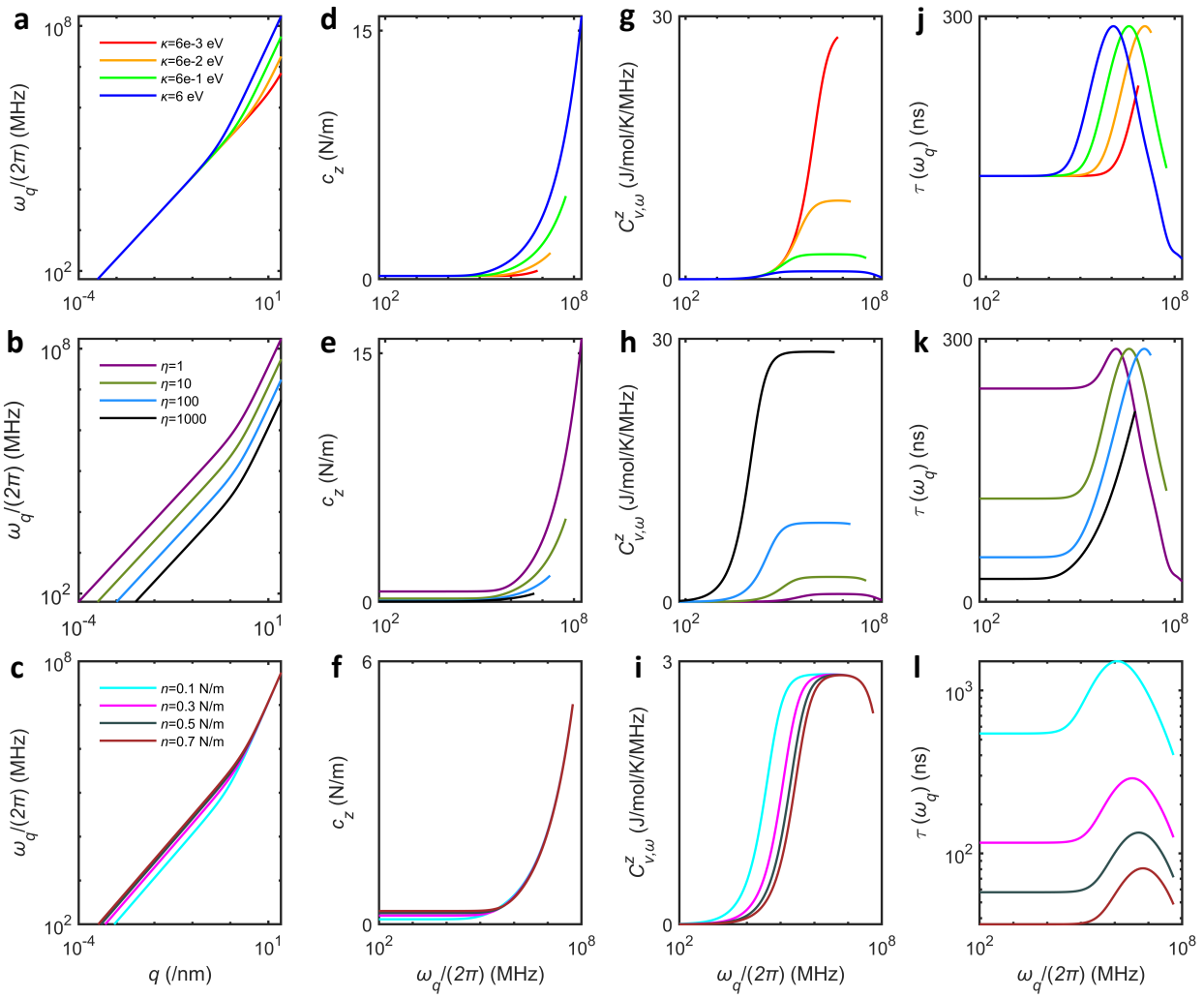

Fig. S5: Discussion for Debye scattering model. Four parameters of flexural acoustic phonons, including frequency ω_q, speed c_z, specific heat spectral density $C^z_{v,\omega}$ and thermal time constant τ are discussed with respect to **a**, bending rigidity κ; **b**, normalized areal mass η; **c**, tension n. Initial settings are $\kappa = 0.6\,\mathrm{eV}$, $\eta = 10$ and $n = 0.3\ \mathrm{N/m}$, and the radius of membrane $r = 5\,\mu\mathrm{m}$.

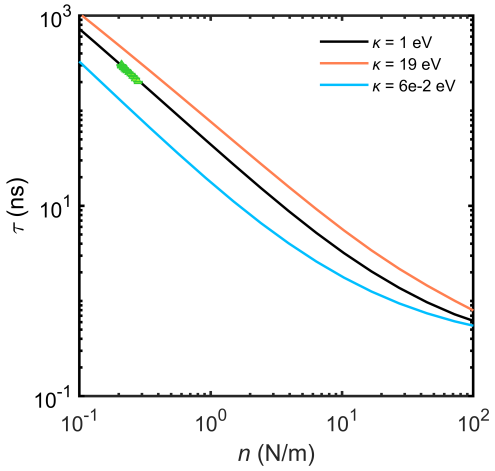

Fig. S6: Influence of bending rigidity on tension-dependent thermal time constant. Green points, measured thermal time constant τ as a function of tension n for device D3 in the main manuscript; lines, estimated τ versus n under different values of κ.

moment.

5 Thermal nonequilibrium of acoustic phonons

Characterizing thermal nonequilibrium among phonons in graphene has recently received a remarkable attention[12–14]. In this work, we consider the absolute value of the thermal expansion forces ratio $|C_{\text{fast}}/C_{\text{slow}}|$. According to the 2D heat equation[3], the thermal expansion amplitude is equal to $\alpha P_{\text{abs}} R$, where α and R is the thermal expansion coefficient and thermal resistance of acoustic phonons, and P_{abs} is the absorbed laser power by the phonons. Assume the values of α are equivalent for all acoustic phonons[15], using $\tau = RC_v$, we have $|C_{\text{fast}}/C_{\text{slow}}| = \gamma \frac{(\tau_l/C_v^l + \tau_t/C_v^t)}{\tau/C_v^z}$, where $\gamma = P_{\text{abs}}^{l,t}/P_{\text{abs}}^{z}$ represents the power absorption ratio between in-plane and flexural phonons. Through the fitting of γ, we obtain a good match between the computed and measured tension-

dependence of $|C_{\text{fast}}/C_{\text{slow}}|$ for all devices (see Fig. 3c in the main manuscript). We express the relative power absorption ξ by flexural phonon as $\xi = 1/(\gamma + 1)$, which is further plotted as the function of η (see Fig. 3d in the main manuscript) to analyze the effect of residues.

References

1. Lopez-Polin, G. *et al.* Increasing the elastic modulus of graphene by controlled defect creation. *Nat. Phys.* **11**, 26–31 (2015).

2. Šiškins, M. *et al.* Sensitive capacitive pressure sensors based on graphene membrane arrays. *Microsyst. Nanoeng.* **6**, 1–9 (2020).

3. Dolleman, R. J. *et al.* Optomechanics for thermal characterization of suspended graphene. *Phys. Rev. B* **96**, 165421 (2017).

4. Dolleman, R. J. *et al.* Transient thermal characterization of suspended monolayer mos 2. *Phys. Rev. Mat.* **2**, 114008 (2018).

5. Dolleman, R. J., Blanter, Y. M., van der Zant, H. S., Steeneken, P. G. & Verbiest, G. J. Phonon scattering at kinks in suspended graphene. *Phys. Rev. B* **101**, 115411 (2020).

6. Lindsay, L., Broido, D. & Mingo, N. Flexural phonons and thermal transport in graphene. *Phys. Rev. B* **82**, 115427 (2010).

7. Lindsay, L., Broido, D. & Mingo, N. Flexural phonons and thermal transport in multilayer graphene and graphite. *Phys. Rev. B* **83**, 235428 (2011).

8. Nika, D. L. & Balandin, A. A. Phonons and thermal transport in graphene and graphene-based materials. *Rep. Prog. Phys.* **80**, 036502 (2017).

9. Nihira, T. & Iwata, T. Temperature dependence of lattice vibrations and analysis of the specific heat of graphite. *Phys. Rev. B* **68**, 134305 (2003).

10. Cong, X. *et al.* Probing the acoustic phonon dispersion and sound velocity of graphene by raman spectroscopy. *Carbon* **149**, 19–24 (2019).

11. Gunst, T., Kaasbjerg, K. & Brandbyge, M. Flexural-phonon scattering induced by electrostatic gating in graphene. *Physical Review Letters* **118**, 046601 (2017).

12. Hunter, N. *et al.* Interface thermal resistance between monolayer wse2 and sio2: Raman probing with consideration of optical–acoustic phonon nonequilibrium. *Adv. Mater. Interfaces* 2102059 (2022).

13. Wang, R. *et al.* Distinguishing optical and acoustic phonon temperatures and their energy coupling factor under photon excitation in nm 2d materials. *Adv. Sci.* **7**, 2000097 (2020).

14. Zobeiri, H., Hunter, N., Wang, R., Wang, T. & Wang, X. Direct characterization of thermal nonequilibrium between optical and acoustic phonons in graphene paper under photon excitation. *Adv. Sci.* **8**, 2004712 (2021).

15. Yang, N., Li, C. & Tang, Y. Effects of chirality and stacking on the thermal expansion effects of graphene. *Mater. Res. Express* **7**, 115001 (2020).